I^5S: Wide-Field Light Microscopy with 100-nm-Scale Resolution in Three Dimensions

Lin Shao,* Berith Isaac,[†‡] Satoru Uzawa,* David A. Agard,*[¶] John W. Sedat,* and Mats G. L. Gustafsson[§]
*Keck Advanced Microscopy Laboratory, Department of Biochemistry and Biophysics, University of California, San Francisco, California; [†]Life Sciences Division, Lawrence Berkeley National Laboratory, Berkeley, California; [‡]Department of Organic Chemistry, Weizmann Institute of Science, Rehovot, Israel; [¶]Howard Hughes Medical Institute; and [§]Department of Physiology and Program in Bioengineering, University of California, San Francisco, California

ABSTRACT A new type of wide-field fluorescence microscopy is described, which produces 100-nm-scale spatial resolution in all three dimensions, by using structured illumination in a microscope that has two opposing objective lenses. Illumination light is split by a grating and a beam splitter into six mutually coherent beams, three of which enter the specimen through each objective lens. The resulting illumination intensity pattern contains high spatial frequency components both axially and laterally. In addition, the emission is collected by both objective lenses coherently, and combined interferometrically on a single camera, resulting in a detection transfer function with axially extended support. These two effects combine to produce near-isotropic resolution. Experimental images of test samples and biological specimens confirm the theoretical predictions.

INTRODUCTION

A considerable number of techniques for enhancing the spatial resolution of light microscopy have been developed over the last two decades (1–20). The number of underlying concepts is much smaller, however, and most of the techniques can be seen as based on these three:

1. Collecting light over a broader set of angles by combining separate apertures (1–3).
2. Using nonuniform illumination light (either a focused beam (4,5) or a periodic pattern (6–13)), by itself or combined with nonlinear photoresponses (4,5,14–16).
3. Precisely locating molecules or particles individually (18–20).

Here we describe a combination of structured illumination microscopy, which is based on concept 2, with I^5M, which uses both concepts 1 and 2.

In structured illumination microscopy (SIM), the sample is illuminated by a periodic pattern, which causes otherwise undetectable high-resolution information to be encoded into the low-resolution observed image in the form of moiré fringes. This information can be computationally extracted to produce an extended-resolution reconstruction (7–12). This method can exceed the conventional resolution by a factor of two in each direction, resulting in a resolution of ~100 nm laterally and 300 nm axially (12). (Even higher resolution is possible by exploiting nonlinear phenomena (14–16); this article considers only the linear case.) The axial resolution thus remains several times worse than the lateral one.

This resolution anisotropy stems from the limited and asymmetric range of light-gathering angles of a normal microscope, in which a single objective lens accesses the sample from one side only. One approach to increase the axial resolution is therefore to increase the set of light-gathering angles by adding a second objective lens on the other side of the sample, and combining the two apertures interferometrically (concept 1, above). This is done in the wide-field technique I^2M (3) and the corresponding point-scanning technique 4Pi-B microscopy (1). The approach is quite similar to interferometric imaging in astronomy (21), in which light from multiple telescopes is combined interferometrically to synthesize a much larger aperture than that of any individual telescope. A separate use of the same geometry is to direct the illumination light through both objective lenses, so that two beams of illumination light interfere at the sample and form an axial interference pattern, which can enhance axial resolution by means of concept 2. Using both types of interference simultaneously results in I^5M (3) and 4Pi-C (1). The wide-field technique I^5M can achieve an axial resolution <100 nm (3), but its lateral resolution equals the conventional one of ~200 nm.

Here we demonstrate a new type of wide-field light microscopy, I^5S, that combines the lateral performance of SIM with the axial performance of I^5M, resulting in a spatial resolution of ~100 nm in all three dimensions. It uses the same opposing-objective-lens geometry as in I^5M (3), but illuminated by the structured-illumination apparatus of three-dimensional SIM (Fig. 1) (12).

THEORY

Within the linear shift-invariant imaging model, the imaging properties of a light microscope can be fully described by

Submitted August 21, 2007, and accepted for publication November 6, 2007.

Address reprint requests to M. G. L. Gustafsson, Tel.: 415-514-4385; E-mail: mats@msg.ucsf.edu.

S. Uzawa's present address is Dept. of Molecular and Cell Biology and Howard Hughes Medical Institute, University of California, Berkeley, CA 94720.

Editor: Enrico Gratton.

0006-3495/08/06/4971/13 $2.00

doi: 10.1529/biophysj.107.120352

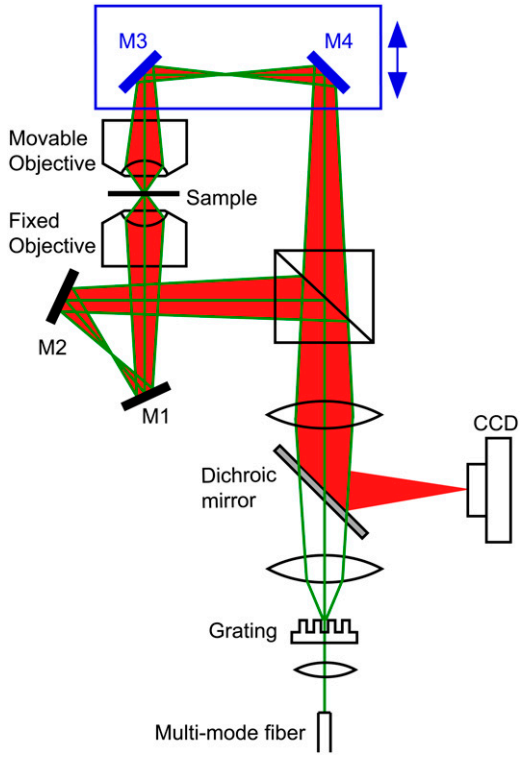

FIGURE 1 A schematic drawing of an I^{5}S microscope. The illumination light passes first through a transmission grating, which diffracts it into three beams (*green lines*), and then through a beam splitter, which splits each beam and directs three beams to each of the two opposing objective lenses. The same beam splitter combines the two beams of emission light (*red*) from the sample onto the camera. The movable objective lens can be positioned in X, Y, and Z with respect to the stationary objective lens. Mirrors M3 and M4 can be translated together to adjust the path-length difference. The grating can be rotated and laterally translated to control the orientation and phase of the illumination pattern.

either the point spread function (PSF) or its Fourier transform, the optical transfer function (OTF). The ultimate resolution limit of a given microscope is determined by the ''support'' of the OTF, the region of three-dimensional reciprocal space where the OTF has nonzero values. An observed image is a convolution of the sample structure with the PSF in real space and therefore, by virtue of the convolution theorem, in reciprocal space its Fourier transform is the pointwise product of the sample's Fourier transform and the OTF. A microscope can thus only detect information from within the OTF support, also known as the observable region (Fig. 2, *A* and *B*). The goal of exceeding the resolution limit is therefore equivalent to devising a microscope that has a larger effective OTF support than the normal observable region.

SIM achieves that goal by moving higher-resolution information into the observable region through spatial frequency mixing with an illumination pattern (7–12). Three-dimensional SIM acts by illuminating the sample with a pattern that has the following properties (12):

i. The illumination pattern is a sum of a finite number of components, each of which is separable as a product of an axial and a lateral function: $I(x,y,z) = \sum_m (I_m(z)J_m(x,y))$.
ii. Each of those lateral functions J_m is a simple harmonic wave (i.e., it has a single spatial frequency).
iii. The axial position of the illumination pattern is fixed in relation to the focal plane of the microscope as the sample is refocused during three-dimensional acquisition.

In the implementation described in Gustafsson et al. (12), the pattern is generated by a one-dimensionally periodic mask, and its phase is controlled by moving the mask laterally as a whole. Under these conditions, the Fourier transform $\tilde{D}$ of the observed image D can be expressed (12) as

$$\tilde{D}(\mathbf{k}) = \sum_{m=-N}^{N} O_m(\mathbf{k})\tilde{S}(\mathbf{k} - m\mathbf{p})e^{im\varphi}. \quad (1)$$

Equation 1 states that the Fourier transform of the observed image is a sum of a finite number of copies of the sample information $\tilde{S}(\mathbf{k})$, each shifted laterally in reciprocal space by a distance $m\mathbf{p}$, filtered by a transfer function O_m, and phase-shifted by a phase $m\varphi$. Here $\mathbf{p}$ is a lateral vector representing the fundamental lateral spatial frequency of the illumination pattern (i.e., the inverse of its lateral period), and O_m is the optical transfer function of the detection system convolved with the axial Fourier transform $\tilde{I}_m$of the axial illumination structure I_m. Equation 1 produces resolution extension by two separate mechanisms: the translation by $m\mathbf{p}$ moves new information laterally into the support of O_m, just like in two-dimensional structured illumination (7−10), but in addition the transfer functions O_m are elongated axially compared to the conventional OTF by the convolution with $\tilde{I}_m$. To use the laterally moved information, the different components $O_m(\mathbf{k})\tilde{S}(\mathbf{k} - m\mathbf{p})$ must be separated. The terms can be separated by acquiring $2N+1$ images of the sample with different phase φ, and then solving a set of $2N+1$ linear equations (12). After separation, the components can be moved back to their true positions in reciprocal space, recombined into a single extended-resolution data set, inverse-filtered, and re-transformed to real space (12).

In three-dimensional SIM, the illumination structure was created by interference among three collimated beams of light, produced as the three central diffraction orders of a transmission phase grating (12). Our implementation of I^{5}S uses the same illumination apparatus, but the three beams are directed through the beam splitter of the interferometric loop of the I^{5}M geometry (Fig. 1). Each beam is thus split in two, resulting in six mutually coherent excitation beams being incident on the sample, one triplet of beams passing through each objective lens (Fig. 1). Each triplet consists of a central beam parallel to the optic axis, and two side beams at an angle β with respect to the optic axis. The direction vectors of all six beams lie within one plane (Fig. 2 *E*). In reciprocal space, the illumination light amplitude thus has six components

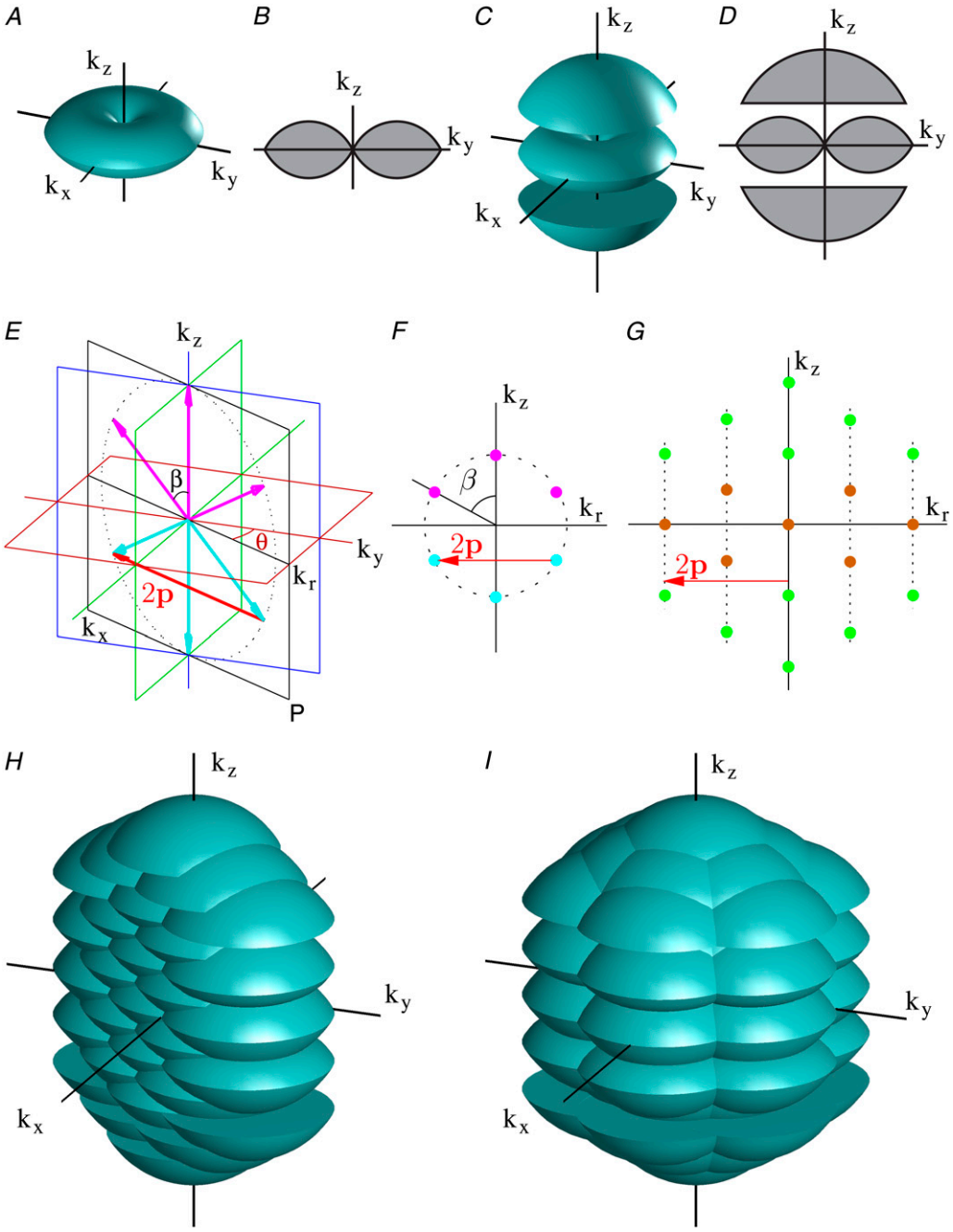

FIGURE 2 Increased OTF support by I^{5}S. (*A–D*) The OTF support for conventional wide-field microscopy (*A* and *B*), and for coherent detection through two opposing objective lenses (*C* and *D*), in three-dimensional rendering (*A* and *C*), and in axial cross section (*B* and *D*). The supports are drawn for monochromatic emission light. (*E–G*) Spatial frequency components of the illumination. I^{5}S uses six mutually coherent illumination beams, three entering through one objective lens (*magenta arrows* in *E*), and three through the other objective lens (*cyan arrows* in *E*). All six beams lie within one plane *P* of frequency space (*black frame* in *E*). (*F*) The corresponding frequency components of the light amplitude, shown within the plane *P*. The six illumination beams interfere pairwise; each pair of amplitude dots in panel *F* gives rise to one illumination intensity component at the position given by the difference vector between the two amplitude dots. This leads to a total of 19 distinct intensity components (*G*). Green dots in panel *G* represent interference between beams that passed through different objective lenses; these are not present in one-objective-lens SIM. (*H*) The effective OTF support produced by the illumination beams shown in panel *E*. This effective support equals a convolution of the detection OTF support in *C* with the illumination intensity in panel *G*. In panel *H*, the resolution extension lies wholly within the plane *P*, but by repeating the procedure with different pattern orientations (different values of the angle θ as defined in *E*), the overall effective OTF support of I^{5}S can be made nearly spherical (*I*).

arranged as shown in Fig. 2 *F*. Since all six beams are mutually coherent, they all interfere with each other pairwise. The resulting intensity pattern therefore contains a frequency component at each difference vector between any two of the amplitude components (12). This leads to 19 frequency components of the illumination intensity, arranged in axial rows at five equally spaced lateral frequencies (Fig. 2 *G*). The resulting real-space illumination structure can be written

$$I(\mathbf{r}_{xy}, z) = \sum_{m=-2}^{2} I_m(z) e^{i(m2\pi \mathbf{p}\cdot\mathbf{r}_{xy} + m\varphi)}, \quad (2)$$

where $\mathbf{r}_{xy}$ represents the lateral coordinates (x, y), $\mathbf{p}$ is the lateral component of the wave vector of each side beam, $I_m(z)$ is a real-space axial function that is the axial Fourier transform of the m^{th} axial row of dots in Fig. 2 *G*, and φ is a phase angle (12). Note that this pattern satisfies conditions i and ii: it is a sum of a finite number (five) of components, each of which is a product of a purely lateral harmonic wave and a purely axial function $I_m(z)$.

If Fig. 2 *G* is compared to the corresponding diagram for three-dimensional SIM using a single objective lens (Fig. 1 *h* of (12)), the only difference is that the latter contains only seven of the 19 intensity components (colored *orange* in Fig. 2 *G*). The additional intensity components in I^{5}S (colored *green* in Fig. 2 *G*) correspond to difference vectors between amplitude components (*dots* in Fig. 2 *F*) that belong to different triplets, that is, they correspond to interference between beams arriving at the sample through different objective lenses. Both techniques involve the same lateral illumination structures $J_m(x,y)$, but their axial illumination structures $I_m(z)$ are quite distinct: the $\tilde{I}_m$ for I^{5}S span a much greater range of axial frequencies k_z, due to their additional intensity components (*dots* in Fig. 2 *G*), and this greater range corresponds to a much greater power to enhance axial resolution.

The illumination structures $\tilde{I}_m$ affect resolution through their effect on the transfer functions O_m: each O_m is produced by a convolution of the detection OTF O with the illumination structure $\tilde{I}_m$ (12), and the k_z extent of $\tilde{I}_m$ determines how much O_m is axially widened by the convolution.

The two-lens geometry not only produces new axial components of the illumination structures $\tilde{I}_m$, but also produces new axial components of the detection OTF O itself, and both these effects contribute to axial broadening of the transfer functions O_m. In I^{5}S, as in I^{5}M, the sample is observed through both objective lenses, and the two beams of detection light are combined interferometrically on a single camera. Interference between these two beams of light creates two side bands in the detection OTF O (Fig. 2, *C* and *D*) (3), which are not present in single-objective-lens microscopy (Fig. 2, *A* and *B*). (Fig. 2, *A–D*, are drawn for a single emission wavelength; the finite emission wavelength bandwidth used in practice will lead to an effective detection OTF support that is the union of a range of single-wavelength OTF supports of slightly different sizes, size being proportional to inverse wavelength. This effect is subtle, since the relative wavelength bandwidth $\delta\lambda/\lambda$ is small.)

The effective OTF support of I^{5}S, taking into account the axially extended span of both $\tilde{I}_m$ and O, and the lateral resolution extension through structured illumination, extends to ~100-nm resolution both axially and laterally (Fig. 2 *H*). A one-dimensional illumination pattern extends the resolution laterally in only one direction—the direction of the pattern. This is seen in Fig. 2 *H* by the OTF support being extended only in the plane defined by the pattern direction and the optic axis (the plane labeled *P* in Fig. 2 *E*). The same resolution improvement can be easily applied in any number of other lateral directions, however, simply by rotating the pattern (changing the angle θ of Fig. 2 *E*) and repeating the procedure, as is done in two-dimensional and three-dimensional SIM (7–12). A sequence of three or more pattern orientations results in an approximately spherical three-dimensional OTF support (Fig. 2 *I*), which translates into a nearly isotropic 100-nm-range resolution.

The regular, latticelike distribution of illumination components depicted in Fig. 2 *G* corresponds to a particular illumination beam angle β (as defined in Fig. 2, *E* and *F*) of 60°. This beam angle is feasible with high-NA objective lenses for oil-, water-, or glycerol-immersion.

The above description, in which the dots in Fig. 2, *F* and *G*, are pointlike, refers to the case when each illumination beam is fully spatially coherent. In the experiments reported here, as in our earlier work on two-dimensional and three-dimensional SIM (9,12), we chose to introduce a slight spatial incoherence into the illumination, to suppress stray interference effects caused by dust particles, etc., in the optical path, and to limit the axial extent on the illumination pattern in sample space. A spatially incoherent light source was simulated by scrambling laser light into a multimode fiber (12); the illumination optics projected three images of the fiber end-face onto the pupil plane of each objective lens (Fig. 3 *A*). Each of the six pointlike amplitude components shown in Fig. 2 *F* therefore turns into a disk of amplitude components (shown in cross section in Fig. 3 *B*). Only identical points of the fiber image are mutually coherent between different beams (an example is shown as *yellow points* in Fig. 3 *A*). The illumination intensity, which is nonzero at every frequency-space point that equals a difference vector between a pair of mutually coherent amplitude components, becomes broadened axially but not laterally: each spot in Fig. 2 *G* turns into an axial line segment (*amber* and *green lines* in Fig. 3 *C*), with the amount of broadening varying between different components, in the same way as happens in one-lens three-dimensional SIM (12). The fact that there are only a discrete number of lateral spatial frequencies is not changed by the incoherence, as long as the objective lens satisfies the Sine Condition (12).

Resolution can be defined in several ways. The most absolute definition is as the extent of the OTF support; this

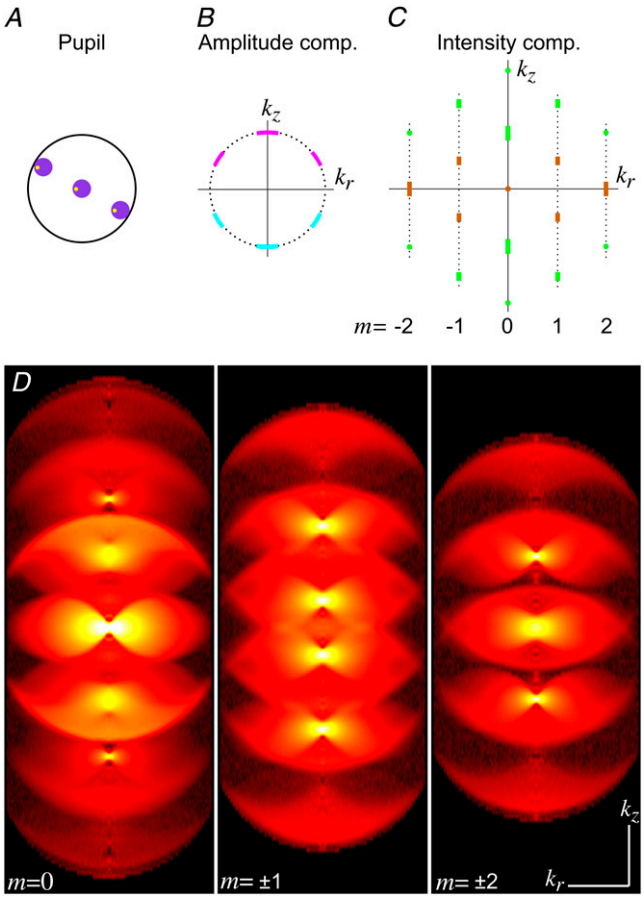

FIGURE 3 The optical transfer functions O_m. (*A*) The illumination projects, onto the back focal plane of each objective lens, three disklike images of the multimode fiber's end face, corresponding to diffraction orders –1, 0, and +1 from the grating. Since the fiber end-face is a spatially incoherent light source, any given point in one of the six fiber images is mutually coherent only with the corresponding point in the other images, and mutually incoherent with all other points (one example of a mutually coherent point triplet in one pupil plane is shown as *yellow points* in *A*). (*B*) The spatial frequency components of the light amplitude forms six circular disks (here shown in cross section), corresponding to the six fiber images, and to the six pointlike dots that occur in the coherent case (Fig. 2 *F*). (*C*) The illumination intensity components, which represent difference vectors between mutually coherent amplitude components, and were pointlike in the coherent case (Fig. 2 *G*), are broadened by the incoherence into axial line segments of differing length. (*D*) Experimentally measured transfer functions O_m for $m = 0, 1, 2$. The image brightness represents the magnitude of $O_m(\mathbf{k})$ as function of $\mathbf{k}$, with a nonlinear color scaling chosen to visualize both strong and weak regions clearly. The measured O_m were rotationally averaged to suppress noise. Each O_m can be visually recognized as a convolution of the corresponding illumination function $\tilde{I}_m$ (*dotted vertical line* in *C*) with the detection OTF (Fig. 2 *D*).

represents the highest spatial frequencies that can be transmitted by the system. In this sense, the predicted resolution of I^{5}S (for NA 1.4 oil immersion objective lenses, excitation and emission wavelengths of 457 nm and 515 nm, respectively, and a pattern spatial frequency of 92.5% of the objective lens's diffraction limit) is 90 nm laterally and 80 nm axially. A second common definition of resolution is as the full width at half-maximum (FWHM) of the effective point spread function. To determine the theoretical resolution of I^{5}S in this sense, we generated a reconstructed image using our standard algorithm, with simulated data of an ideal point source as the input. The ideal point source data were simulated based on the measured I^{5}S OTF (see Methods), which represents a rotationally averaged point source image. The axial and lateral FWHM of the resulting reconstructed bead image were 97 nm laterally and 80 nm axially.

METHODS

Microscope

Our implementation of an I^{5}S microscope, as schematically shown in Fig. 1, is a straightforward combination of the two-objective-lens interferometer used in I^{5}M (3) and the structured-illumination apparatus from three-dimensional SIM (12). Laser light at 457 or 532 nm is scrambled by a rotating diffuser, coupled through a multimode fiber, collimated, and directed to a fused silica linear transmission grating. Diffraction orders –1, 0, and +1 from the grating are passed through a beam splitter, which directs three beams to each of two opposing objective lenses. One of the objective lenses is piezoelectrically translatable in *X*, *Y*, and *Z*, and manually adjustable in tip and tilt angles, with respect to the other objective lens.

Emission light from the sample is collected by both objective lenses, combined by the same beam splitter, and directed onto a single camera by a dichroic mirror via an emission filter wheel (emission filter band 515 ± 15 nm and 605 ± 25 nm for green and red emissions, respectively). The difference in optical path length between the two light paths from the common focal plane of the objective lenses to the beam splitter can be adjusted by moving a translation stage on which two mirrors (M3 and M4 in Fig. 1) are mounted. The phase and orientation of the lateral illumination pattern are adjusted by translating and rotating the grating. The grating is held on a piezoelectric translator, which is mounted on a motorized rotation stage together with a co-rotating linear polarizer. All six linear degrees of freedom (objective lens *XYZ*, path-length difference, grating phase, and sample focus) are piezoelectrically actuated under closed-loop control based on capacitive position sensing (3,8,12).

Two laser tools are used for automatic alignment maintenance, to decrease the influence of thermal drift. To monitor the relative alignment of the objective lenses, light from a fixed point source is focused near the focal plane (through mirror M3 in Fig. 1, which is slightly transparent) by the movable objective lens, and reimaged onto the camera by the fixed objective lens via the beam splitter. A wedged multiple-reflection device, which resides in the emission filter wheel and can be rapidly swung into the beam path, splits the image into several spots with different focus; the positions and diameter ratios of the spots indicate the *XY* and *Z* alignment, respectively, between the two objective lenses. To monitor the path-length difference, infrared light is directed into the interferometric loop through the fourth face of the beam splitter (its *right side* in Fig. 1) and is reflected by separate dichroic infrared reflectors mounted behind each objective lens. The two reflected beams generate lateral interference fringes when combined on the camera, as the reflectors are intentionally not quite parallel; any changes in path length (except within the objective lenses and sample area) are indicated by phase changes of the fringes. The process of rotating the filter wheel, acquiring and evaluating alignment data, and automatically actuating the alignment corrections takes <1 s, and can be interspersed into data set acquisition sequences if desired.

Sample preparation

Bead samples were prepared by depositing a drop of microsphere suspension (FluoSpheres, Invitrogen, Carlsbad, CA), diluted in water, onto a heated

cover glass, and allowing the water to evaporate. The cover glass was mounted in microscope immersion fluid (Laser Liquid 5610, Cargille Labs, Cedar Grove, NJ), backed with another smaller cover glass, and sealed with clear nail polish.

HeLa cells were grown on cover glasses and fixed using a standard protocol (22). The fixed cells were stained with anti-α-tubulin primary antibody (DM1A, Sigma-Aldrich, St. Louis, MO) followed by AlexaFluor-488-labeled secondary antibody (Invitrogen). To provide a mounting medium that was well matched to the design refractive index of the oil-immersion lenses used, the cells were mounted in Laser Liquid as follows. The fixed and stained sample was postfixed in 4% formaldehyde and stepped first into acetone via a series of intermediate mixtures (20% acetone in buffer, followed by 40, 60, and 80% acetone in water, and 100% acetone), 5 min for each step, and then through a series of acetone-Laser Liquid mixtures with increasing Laser Liquid concentration from 20% to 100%. The cover glass was then backed by a smaller cover glass and sealed with nail polish.

Meiotic chromosomes of *C. elegans* were prepared using a protocol developed for electron microscopy (EM) (23). Gravid hermaphrodite worms were high-pressure frozen at liquid nitrogen temperature and freeze-substituted with 0.2% ethylene glycol bis[succinimidylsuccinate] (Pierce Biotechnology, Rockford, IL) dissolved in anhydrous acetone. The sample was returned to room temperature and gradually infiltrated with Epon resin. After curing of the resin on a slide glass, the part containing the gonad was cut out as a small block, which was serially sectioned into 2.5-μm-thick sections. Sections containing germ cells in the pachytene stage of meiosis were identified for imaging. For staining, the sections were immersed for 12 h in a solution of OliGreen (Invitrogen). This procedure stained chromatin throughout the thickness of the slabs, while staining cytoplasmic RNA mainly near the periphery of the sections (see Fig. 7, *C* and *F*). The stained slabs were mounted in Laser Liquid between two cover glasses.

It should be noted that these special mounting protocols were chosen only to achieve index matching between the mounting media and the design immersion medium of the particular objective type (oil immersion) that was available for our prototype. While high-pressure freezing is an excellent method to achieve EM-level structural preservation, simpler protocols may be preferred. If an I^{5}S microscope was instead designed around high-NA water- or glycerol-immersion objective lenses, index matching could be achieved with standard water- or glycerol-based mounting media. A water-miscible high-index mounting medium has recently been described (24), which could simplify sample preparation even in the case of oil-immersion objective lenses.

Alignment

The phases of the axial interference effects are determined by the difference in optical path length between the two branches of the interferometric loop (from the focal plane to the beam splitter). For maximum interference contrast, this difference should be small compared to the coherence length of the light, and for fully constructive interference the difference should be equal to a multiple of the wavelength. The ideal condition, of course, is zero path-length difference. We align the system so that the path-length difference is zero to a precision of a small fraction of a wavelength. As a coarse alignment step, we plot the image intensity (under laterally uniform, I^{5}M-type illumination) of some in-focus, axially point- or line-like object while changing the path-length difference by moving the translation stage that carries mirrors M3 and M4 (Fig. 1). The ability to make large changes of path-length difference without affecting other alignment parameters is the main advantage of the five-reflection geometry shown in Fig. 1, relative to the triangular geometry of commercial 4Pi microscopes. The strongest peak of this oscillating plot represents the ''zero path difference fringe,'' and the corresponding phase stage position is picked. Immediately before each data set is started, a fine alignment step is performed, to locate the peak of this fringe. This is done by recording the axial profile of the point- or line-like sample feature; at perfect phase alignment, this profile should exhibit side lobes of equal height above and below focus. The preparation before each data set also includes fine-aligning the two objective lenses to each other in x, y, and z.

The phase tilt (i.e., the tilt of the axial interference fringes relative to the focal plane, which is related to the lateral alignment of the aperture planes of the two objective lenses to each other as seen from the light source (or camera)) is comparatively stable and is typically left untouched for weeks. It can be tuned by angularly adjusting mirror M2 while compensating with mirror M1 to prevent lateral image shift (Fig. 1).

It is not possible to perfectly eliminate the phase over the entire image, because of a nonlinearly position-dependent phase error (corresponding to nonflatness of the axial interference fringes), which we attribute to less-than-perfect wavefront quality of the beam splitter cube. Within a 300×300 pixel sub-area ($\rightarrow 600 \times 600$ pixels in the reconstruction), however, this error is small enough to neglect. Modest position-dependent phase errors could be compensated for in the processing if they are consistent and known.

The focal planes of the two objectives are made parallel by adjusting the tip and tilt angles of the movable objective. This parameter was only adjusted once after initial assembly or major system revisions.

Image acquisition and reconstruction

Image acquisition was performed in the same manner as in three-dimensional SIM (12), except that the increased axial resolution required the focal step to be reduced to 36.6 nm when in I^{5}S mode, to maintain Nyquist sampling. Automatic alignment correction as described above was interspersed during acquisition of the biological data sets shown later in Figs. 6 and 7, but not the bead data sets shown in Figs. 3–5. Image reconstruction followed the algorithm described for three-dimensional SIM (12). PSF data were acquired experimentally by using a subresolution fluorescent bead (50-nm-diameter FluoSphere, Invitrogen) as an approximation of a point object. It should be noted that the drastically improved axial resolution (the extended axial support of the transfer functions O_m) places a constraint on the bead size. The measured OTF is the true OTF multiplied by the Fourier transform $\tilde{H}$ of the shape of the bead, so the first zero of $\tilde{H}$ must lie well outside the OTF support for the measurement to yield a good measure of the OTF. This is the case for I^{5}S when using a 50-nm-diameter bead, but not when using more conventional 100–120-nm beads. Even this smaller bead size has a residual effect on the measurement, but it can be compensated for simply by dividing the measured OTF by $\tilde{H}$. PSF data were acquired for five different phases of the illumination pattern, and the Fourier-transformed PSF data were separated into the different transfer function orders O_m using the same phase-shift method as in two-dimensional and three-dimensional SIM (8,9,12). Each measured O_m was rotationally averaged around the k_z axis to suppress noise. Only three O_m need to be recorded, because of symmetry: $O_{-\mathrm{m}}(\mathbf{k}) = O_\mathrm{m}(\mathbf{k})$.

Acquisition of the data set used for Fig. 6, which contains 80 axial sections of 300×300 pixels (each at five phases and three pattern orientations) and used 80–100-ms variable exposure time, required 25 min on a microscope that was based on an old camera with slow data readout. A modernized prototype with a somewhat faster camera has since been constructed, which can acquire a similar-sized data set in 4 min 33 s. Reconstruction of a data set of that size, resulting in a $600 \times 600 \times 80$ voxel reconstruction, required 80 s on a computer with two dual-core 2.2 GHz Opteron processors. This processing time includes extensive parameter fitting (12); with a well-characterized and reproducible microscope, most of the parameters could be considered known, which would speed up the processing considerably.

RESULTS

OTF measurement

The measured I^{5}S OTFs (O_m in Eq. 1 for $m = 0$ to 2) are shown in Fig. 3 *D*. Their general appearance is in excellent agreement with expectations. Each O_m can be recognized as a convolution of its corresponding axial illumination function $\tilde{I}_\mathrm{m}$ (*dotted vertical lines* in Fig. 3 *C*) with the three-lobed detection OTF

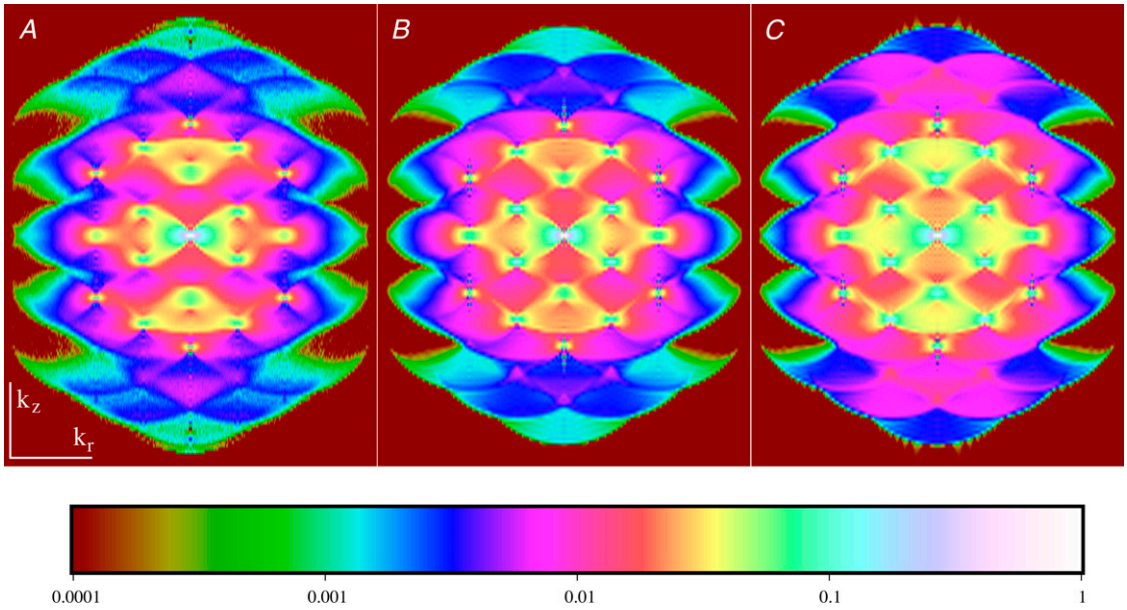

FIGURE 4 A comparison between experimentally measured (*A*) and theoretically calculated (*B* and *C*) optical transfer functions (OTF) of I^5S. Images show the magnitude of the OTF values in the k_z–k_r plane (see Fig. 2 *E*). The same color map (shown in *logarithmic scale* at the *bottom*) is used for all figures. For panel *A*, the three orders of OTFs were separated from measured PSF data as described in Methods, rotationally averaged to suppress noise, and assembled according to Eq. 3. For panels *B* and *C*, a theoretical I^2M PSF was first calculated, multiplied by a calculated real-space illumination pattern, and Fourier-transformed. Panel *C* represents a fully ideal situation, whereas in panel *B* one parameter, representing the contrast of the axial interference effects, was adjusted to match the measured OTF. The correspondence of the experimentally measured I^5S OTF in panel *A* to the theoretical calculations, especially panel *B*, is generally excellent. The ideal calculation in panel *C* indicates that an improved instrument could get somewhat higher signal at high axial spatial frequencies. (The low numerical values are due to the OTFs being normalized to their divergent peak at the origin of frequency space; this peak is finite only because of the finite calculation volume.)

(Fig. 2, *C* and *D*). Each intensity component (*amber* or *green dot* or *line segment* in Fig. 3 *C*) of an illumination function $\tilde{I}_m$ contributes one (possibly axially broadened) copy of the detection OTF to the corresponding O_m in Fig. 3 *D*. In particular, it can be seen that those intensity components that are expected to be significantly broadened axially, due to the spatial incoherence of the illumination, do produce correspondingly broadened detection-OTF copies in Fig. 3 *D*.

Fig. 4 *A* shows the experimentally measured total effective OTF of I^5S (for a single orientation of the illumination pattern), computationally reassembled from the measured component OTFs O_m as

$$OTF_{\text{eff}}(\mathbf{k}) = \sqrt{\sum_{m=-2}^{2} |O_m(\mathbf{k} - m\mathbf{p})|^2}. \quad (3)$$

This measured OTF should be compared to the purely theoretical OTFs shown in Fig. 4, *B* and *C*. These theoretical OTFs were constructed by:

1. Calculating an ideal theoretical detection PSF using a vectorial imaging model (25), assuming a single wavelength and an NA of 1.35, which best matched the observations.
2. Calculating the expected real-space illumination pattern (*I* of Eq. 2), assuming an ideal objective lens that satisfies the Sine Condition and using the experimental values of the lateral pattern frequency and the ratio of the fiber image diameter to the pupil diameter.
3. Multiplying the calculated detection PSF with *I*.
4. Fourier-transforming the result.

The calculation in Fig. 4 *C* assumed fully ideal conditions, whereas that in Fig. 4 *B* was fitted to the experimental data using a single adjustable parameter that represented the contrast of the axial interference effects. This contrast was incomplete in the experiment, due to nonideal optical components: the intensities of the two beam triplets were not equal, because of a nonideal split ratio of the beam splitter and inequivalent mirror reflection losses of the two paths due to inequivalent mirror angles; furthermore, the beams were not perfectly *s*-polarized when they reached the sample, because of polarization-dependent reflectivities and undesired retardance, especially of the beam splitter but also of the mirrors. Metal-based reflective components were used, to minimize such retardance effects. The measured result matches the theoretical calculation quite closely, especially after this one parameter has been taken into account (Fig. 4 *B*). Ideal components would considerably improve the signal level at high axial spatial frequencies (Fig. 4 *C*).

Bead cluster

To demonstrate the performance of I^5S, we prepared a test sample containing a mixture of red and green fluorescent beads of 120-nm nominal diameter, and imaged the red beads

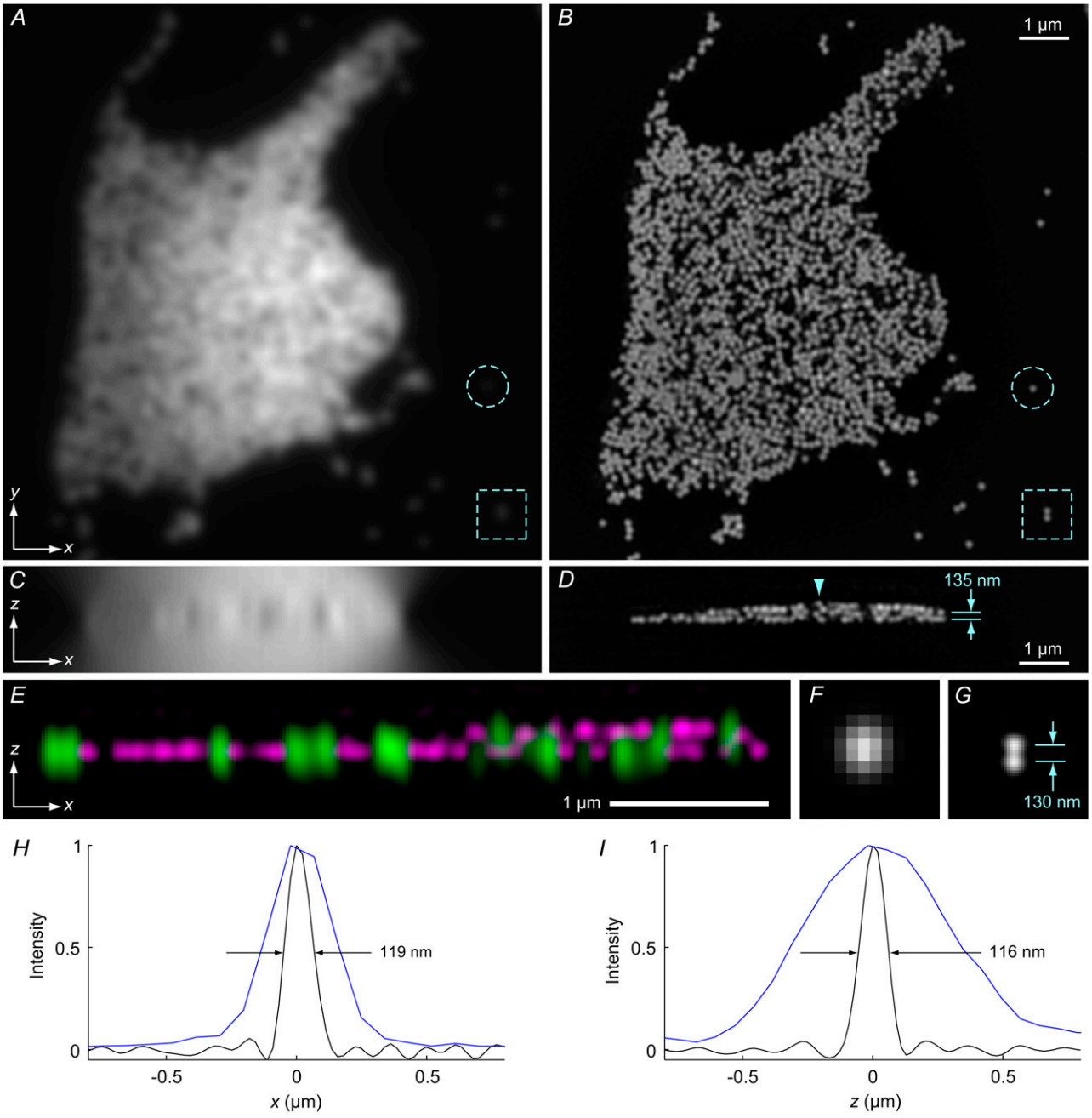

FIGURE 5 Comparison of resolving power on a cluster of mixed red and green fluorescent beads. Corresponding single lateral (*A* and *B*) and axial (*C* and *D*) sections of the red channel illustrate the resolution improvement and true three-dimensional imaging achieved by I^5S (*B* and *D*) compared to conventional microscopy (*A* and *C*). Individual beads can be distinguished even where there are several close-packed layers (*D*, *arrowhead*), and pairs of adjacent beads are well resolved at ~135 nm axial center-to-center distance (*D*, *arrows*). (*E*) An *x*,*z* section in which red beads (displayed here in *magenta*) are imaged and reconstructed by I^5S, and green beads by single-objective-lens three-dimensional SIM, for comparison of axial resolution. The apparent axial full width at half-maximum (FWHM) of the green beads is ~300 nm. (*F* and *G*) Contrast-adjusted enlargements of the boxed area of panels *A* and *B*, respectively, which contained two beads separated laterally by ~130 nm. (*H* and *I*) Normalized intensity profiles, along the *x* and *z* direction, respectively, through an isolated bead (*circled* in *A* and *B*), using I^5S (*black curves*) or conventional microscopy (*blue curves*). The FWHM measured from the I^5S profiles is 119 nm laterally and 116 nm axially. All data were acquired with the lateral pixel size shown in panel *F*, 90.4 nm, and a *z* step of 36.6 nm (I^5S) or 73.2 nm (conventional). The pixel dimensions of the I^5S reconstructions were subdivided by factors of four laterally and two axially during processing; panels *A* and *C* have been interpolated to the same pixel dimensions for easier comparison.

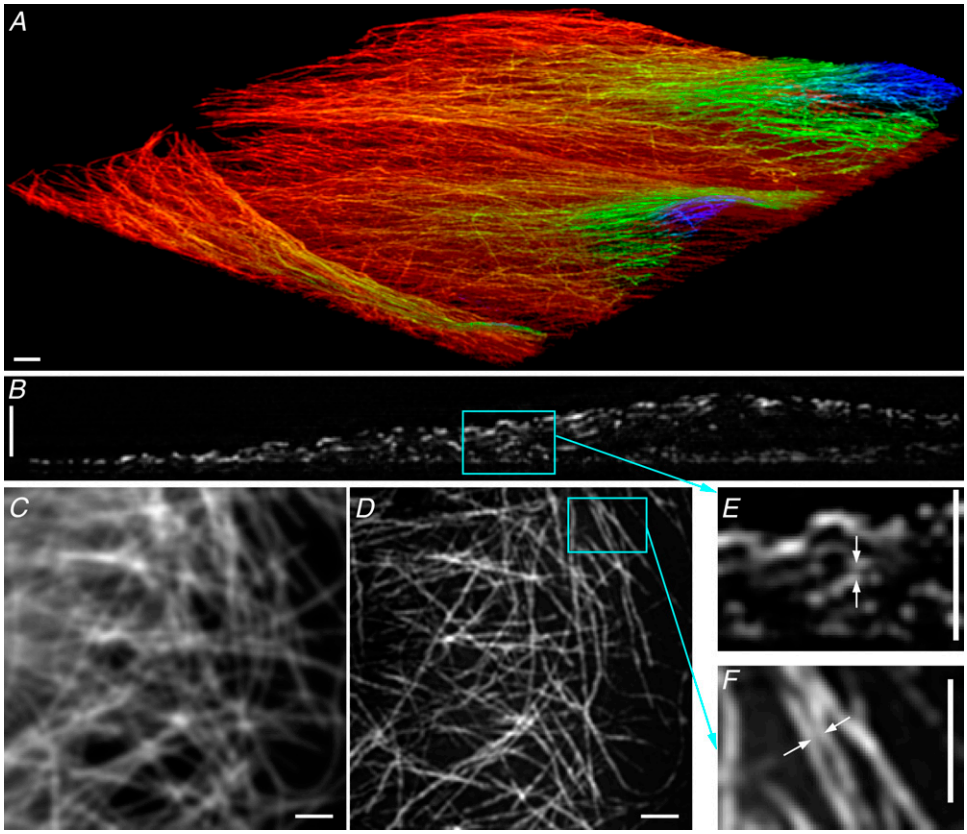

FIGURE 6 The microtubule cytoskeleton in HeLa cells, immunofluorescently labeled and imaged by I^5S. (*A*) A three-dimensional rendering of a maximum-intensity projection through the reconstructed data set, which captured portions of three neighboring cells. The hue indicates the axial position of each point: red-green-blue correspond to increasing distance from the cover glass. (*B*) A single axial (*y*,*z*) section through the volume. The subregion inside the green box in panel *B* is shown magnified in panel *E*, where the separation between the two parallel microtubules pointed to by the arrows is 106 nm. (*C* and *D*) Comparison of lateral resolution between conventional microscopy (*C*) and I^5S (*D*), using one lateral section from the volume. (*F*) Magnified version of the boxed region in panel *D*, where the separation between the two microtubules pointed to by arrows is 120 nm. (All scale bars: 1 μm.) A video of this reconstruction is available on the journal web site (Movie S1).

by I^5S (Fig. 5, *B* and *D*). For comparison, the same sample was reimaged using the same microscope working in the conventional wide-field mode (Fig. 5, *A* and *C*).

Fig. 5, *A* and *B*, illustrate the substantial improvement of lateral resolution that I^5S has in common with other forms of structured-illumination microscopy (8,9,12). For example, a pair of beads spaced 130 nm apart laterally are well resolved by I^5S even at this red emission wavelength (Fig. 5 *G*) whereas they appear as a single object in the conventional image (Fig. 5 *F*).

What is unique about I^5S, however, is that this lateral resolution is accompanied by an equally high axial resolution performance. The bead cluster imaged in Fig. 5 actually consisted of several layers of 120-nm beads; the conventional image in Fig. 5 *A* represents the sum of all layers, since all the layers lie well within the depth of field of the conventional microscope. Fig. 5 *B*, however, which represents a single *z* level from the I^5S reconstruction, contains information from only a single layer of beads. The image is unaffected by the presence of the next bead layer located a mere 98 nm away (the bead diameter of 120 nm times a geometric factor of $\sqrt{2/3}$ for the layer spacing of close-packed spheres).

Axial sections through the same data set illustrate an even more pronounced difference between I^5S and conventional microscopy. Out-of-focus blur dominates the conventional data set above and below the bead layer (Fig. 5 *C*), but is absent from the I^5S reconstruction (Fig. 5 *D*). The out-of-focus blur is computationally removed by the reconstruction process; this is possible because the laterally moved information provides information within the so-called missing cone of frequency space. Thus I^5S, like single-lens three-dimensional SIM, provides true three-dimensional imaging (optical sectioning).

Whereas the blur-removal property of I^5S is similar to that of single-lens SIM, its axial resolving power is vastly superior. Beads located only 135 nm apart axially are well resolved (Fig. 5 *D*, *arrows*), and beads in adjacent close-packed layers are reconstructed as separate even where several layer are stacked (Fig. 5 *D*, *arrowhead*).

Fig. 5 *E* shows another *x*,*z* section, where two layers of red beads are easily distinguished. In this panel the green beads are also displayed, but imaged with single-objective-lens three-dimensional SIM. The axial resolution achieved on the green beads, ~300 nm FWHM, is already a factor-of-two improvement over conventional microscopes, but it is immediately obvious from the image that the resolution achieved by I^5S on the red beads is much higher still.

To quantify the resolution properties, we plotted lateral and axial intensity profiles (Fig. 5, *F* and *G*) through an isolated single bead (*circled* in Fig. 5, *A* and *B*). The lateral and axial FWHM measured from these profiles were 119 nm and 116 nm, respectively. In comparing these values to the theoretical predictions made in Theory, the different wavelength values must be taken into account. Scaling of the measured FWHM values to the wavelengths used in the theoretical prediction yields 102.2 nm laterally and 99.6 nm axially.

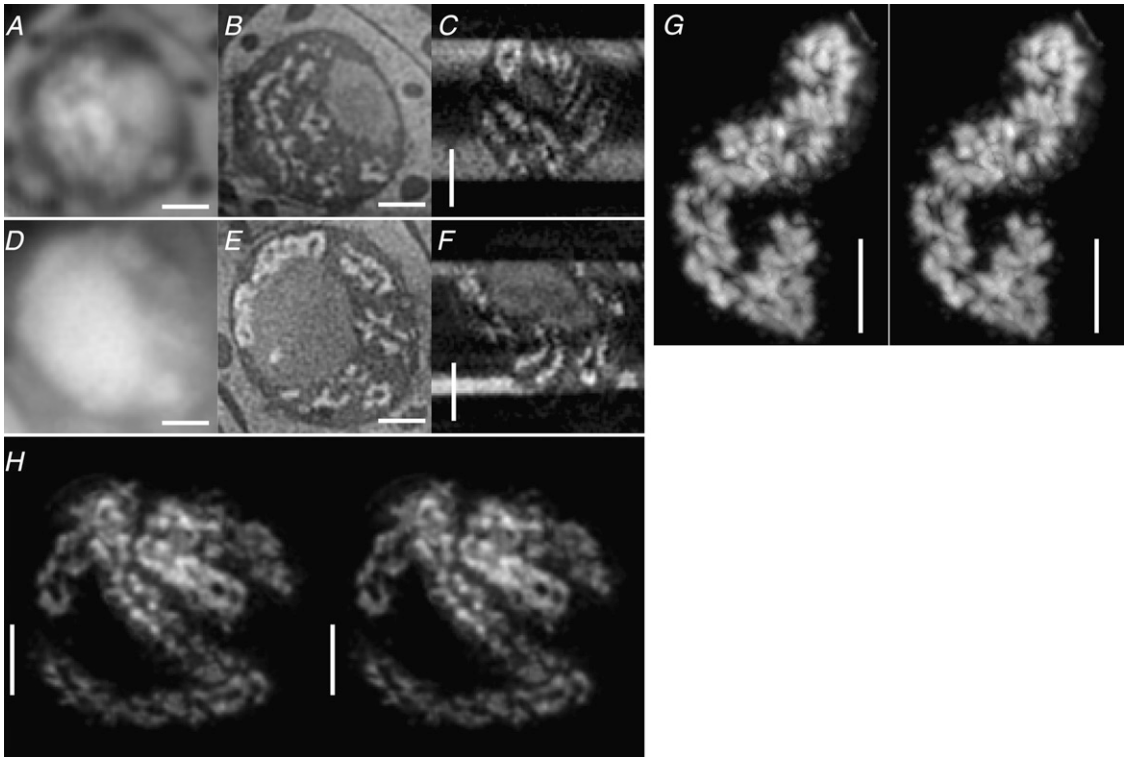

FIGURE 7 Meiotic cells from a *C. elegans* gonad that was high-pressure frozen, freeze-substituted, resin-embedded, sectioned, stained for DNA/RNA with OliGreen, and imaged with I^5S. Panels *A–C* and *D–E* show two different cells, in lateral sections with conventional microscopy (*A* and *D*) or I^5S (*B* and *E*), and axial sections with I^5S (*C* and *F*). Chromosomes and the nucleolus were stained throughout the volume, whereas cytoplasmic RNA was stained only near the edges of the resin section (*C* and *F*). (*G*) A cross-eyed stereo pair rendering of a maximum-intensity projection of one computationally isolated chromosome. A video of this reconstruction is available on the journal web site (Movie S2). (*H*) A similar stereo pair showing several chromosomes within a single nucleus. (All scale bars: 1 μm.)

HeLa cell microtubules

To test the performance of I^5S on biological samples, we imaged the microtubule cytoskeleton in HeLa cells (Fig. 6, Supplementary Material, Data S1, Movie S1). Shown in Fig. 6 *A* is a maximum-intensity projection of a three-dimensional volume reconstructed with I^5S for one such sample. Parts of three neighboring cells are captured in this volume. For clarity, the axial position of each point in the volume is color-coded. The flat bottom plane where the cells adhere to the cover glass corresponds to red color, whereas green and blue hues indicate increasing distance from the cover glass. The right side of the volume intersects the cells' nuclei, which appear, as expected, as microtubule-free cavities. As can be seen, the three-dimensional structure of the cytoskeleton is distinctly delineated by I^5S. Adjacent microtubules are well resolved at 106-nm axial separation (Fig. 6 *E*), and at 120-nm lateral separation (Fig. 6 *F*).

Meiotic chromosomes of *C. elegans*

I^5S was also used to image meiotic chromosomes in a *C. elegans* gonad that had been prepared as for electron microscopy (23) (Fig. 7, Movie S2). The meiotic chromosomes are seen confined to the periphery of the nucleus, wrapping around the nucleolus, with approximately the same high resolution in both lateral (Fig. 7, *B* and *E*) and axial sections (Fig. 7, *C* and *F*). Large cytoplasmic organelles, presumably mitochondria, can be seen as sharply defined voids in the RNA signal (Fig. 7 *B*). Stereo pair maximum-intensity projections of a computationally isolated individual chromosome (Fig. 7 *G*) and of a congregation of chromosomes (Fig. 7 *H*) demonstrate the potential of I^5S in the study of subcellular ultrastructure at the 100-nm resolution level.

DISCUSSION

To clarify the possible role for I^5S in microscopy, we will here outline its relationships to existing high-resolution techniques.

Compared to transmission EM, scanning EM, and the various scanned probe microscopies, I^5S like other fluorescence microscopy offers highly specific labeling of biomolecules in multiple colors, and three-dimensional imaging of the interior of samples that are thicker than the typically submicron slices accessible to transmission EM tomography and the even thinner surface layers probed by the scanned techniques. Compared to any other linear light microscope modes, the interferometric dual-objective-lens methods I^5S, 4Pi, and I^5M provide much higher axial resolution.

The internal relationships between I^5S, 4Pi, and I^5M are somewhat analogous to those between single-lens SIM, confocal microscopy, and conventional wide-field microscopy. Both I^5S and 4Pi in principle benefit from the same factor-of-two increase in lateral resolution compared to conventional microscopy, as do other methods that involve nonuniform illumination, including single-lens SIM and confocal microscopy. Their relative performance depends on several parameters including the thickness, sparseness, and brightness of the sample. Structured-illumination methods such as I^5S provide higher signal level of high-lateral-resolution information than point-scanning methods like 4Pi do, because they concentrate much of their illumination energy at the largest angles that contribute most strongly to encoding high-resolution information, whereas point-scanning methods spread their illumination energy over all available illumination angles. On the other hand, pinhole-based scanning methods provide better signal/noise in the limit of very thick and densely fluorescent samples, because they exclude out-of-focus light physically rather than computationally. Computationally removed out-of-focus light leaves behind its shot noise, so image data that is overwhelmingly dominated by out-of-focus light can yield noisy reconstructions. Therefore there will be a threshold of thickness and denseness below which structured illumination methods will provide better resolution, and above which confocal methods will be preferable. Because the whole class of interferometric dual-objective-lens methods to which I^5S and 4Pi belong requires samples to be thin and optically uniform enough that a given focal plane can be imaged near-perfectly from both sides, we expect typical applications of such methods to lie below that threshold, where I^5S would yield the better effective resolution compared to 4Pi. Comparisons are complicated by several other factors: wide-field methods like I^5S can use charge-coupled device cameras, which can have $>90\%$ quantum efficiency at visible wavelengths, whereas point-scanning methods typically detect the light with photomultiplier tubes that have considerably lower quantum efficiency. (Some point-scanning microscopes, including commercial 4Pi systems, can instead use avalanche photodiodes, which have intermediate quantum efficiency—typically 45–60% in the green, 60–70% in the red—but have data rate limitations.) Higher quantum efficiency leads to higher photon counts and thereby to lower relative shot noise in the signal. On the other hand, 4Pi methods, at least those using two-photon excitation, benefit from a more uniform optical transfer function, which decreases the demands on the noise level (26).

As described here, I^5S, and three-dimensional SIM in general, involve illumination intensity structures that contain multiple frequency components simultaneously. As an alternative approach, it is also possible to access the same total amount of information by applying one illumination spatial frequency at a time, sequentially. This general concept is equivalent to two-dimensional SIM if applied purely laterally, and to the original form of standing wave fluorescence microscopy (6) if applied purely axially. More general forms, using sequences of oblique pattern directions, have been proposed (11,27,28), including three-dimensional harmonic excitation light microscopy (11). Compared to these sequential single-frequency methods, I^5S greatly simplifies the microscope hardware and acquisition by decreasing the number of separate illumination patterns that need to be applied. It also improves axial resolution further, by benefiting from interference effects in the emission light in addition to those that generate the illumination pattern, thereby changing the detection OTF support from that in Fig. 2, *A* and *B*, to the larger one shown in Fig. 2, *C* and *D*. Even though single illumination frequencies that are neither purely axial nor purely lateral do not satisfy the conditions i–iii that led to Eq. 1 (see Theory), they can be treated using essentially the same method. The only differences are that the phase shifts of the pattern take place in the pattern direction instead of being purely lateral, that the information shift vector $\mathbf{p}$ is also not purely lateral, and that the detection OTF is not broadened by any axial illumination structure.

Iterative deconvolution (29), a common tool in three-dimensional light microscopy, could also be applied to I^5S data, and may be quite helpful given the rugged OTF landscape (Fig. 4). To avoid any ambiguity about whether any of the observed resolution improvement could be attributable to constrained algorithms, we have made no use of constraints in this article, and instead used a linear processing algorithm that provides a well-defined, position-independent effective PSF.

The OTF supports, and therefore the theoretical resolution limits, of I^5S or 4Pi-C are close to the maximum possible through linear, far-field visible-light means. If the sample can be made to have a nonlinear photoresponse, however, much higher resolution is possible. This concept (14,30) has been demonstrated both in the point-scanning context (5), and for wide-field microscopy using periodic patterns (15,16). Can the axial resolution enhancement of the I^5S geometry be combined with the theoretically unlimited resolution achievable with nonlinear methods? In principle, the answer is yes: the methods are fully compatible and complementary, and the nonlinearity would further extend the axial resolution in much the same way as the lateral one. A similar combination has been demonstrated in the point-scanning context, by combining 4Pi microscopy with STED (31). The challenge in practice would be the large number of images required, which would require the fluorophores to be highly photostable to keep photobleaching within acceptable levels. If photostability is limiting, as is often the case in fluorescence microscopy in general, the axial information gained by I^5S, or indeed by any form of three-dimensional imaging that involves a focal series of images, may require a tradeoff against the lateral resolution: the total acceptable exposure of the sample would be divided among a number of focal planes, leading to lower numbers of in-focus photons detected in any given plane.

All the methods described so far treat the unknown sample as a continuous distribution of fluorescent dye. In reality, the sample consists of a finite (though typically very large) number of individual molecules, each of which undergoes discrete stochastic events such as blinking and photobleaching. At extreme resolution, when each resolution volume may contain only a small number of fluorophores, the molecular discreteness may have subtle effects on the data. In the methods directed at continuous distributions, such effects may merely constitute a nuisance, but there is a separate category of high-resolution methods that embrace the discrete nature of the sample and exploit it as a path to high resolution. These methods seek to identify the position of each molecule with high precision, by forming an image of it in isolation from its neighbors, and determining the center of that image. Limited isolation can be achieved spectrally (32), especially at cryogenic temperatures (17), or by exploiting the discreteness of photobleaching (33) or blinking (34). Recently, very high resolution has been achieved by applying this concept to the stochastic activation of photoactivatable fluorophores (18–20). Such methods can reach extreme levels of resolution, at the cost of requiring many thousands of individual images (18) for a single two-dimensional output image. Similarly as for nonlinear structured illumination, three-dimensional extension of the same concept is possible in principle, but likely at a tradeoff against lateral resolution.

One limitation, which is shared by all the dual-objective-lens methods, is the requirement that the sample be sufficiently thin and/or optically homogeneous to allow near-ideal imaging from both sides. Encouraging results with 4Pi, where for example only subtle phase differences were observed when comparing lightpaths that passed either through or adjacent to a 13-μm-thick live nucleus (35), indicate that this condition may be less restrictive than originally thought. A second challenge of I^5S in its prototype form involves the engineering task of keeping the objective lenses and the interferometric loop aligned during acquisition. Alignment maintenance could be greatly simplified by housing the interferometric loop in a compact, intrinsically stable imaging head, and by using direct optical sensing of the alignment parameters for feedback. (For example, the latter concept could mean eliminating the capacitive sensing, and instead using, as the primary sensor for closed-loop alignment control, a real-time version of the optical system that was here used for secondary alignment maintenance.) Commercially available systems intended for 4Pi confocal microscopy could provide a simplified route to I^5S, since the interferometric loop itself is identical between the two techniques.

In summary, we believe that I^5S will serve a class of questions that require an isotropic three-dimensional resolution in the 100-nm regime, and can be addressed in fixed or quiescent samples, but involve a sample thickness or labeling complexity that is impractical with electron microscopy. One example of such a question is the long-standing problem of mitotic chromosome structure (36), for which conventional or confocal microscopes have insufficient resolution, and electron microscopes lack the necessary specificity of labeling. It is our hope that the size-scale gap that has classically existed between optical and electron-based three-dimensional microscopy can be bridged by the emerging class of high-resolution light microscopies, including I^5S.

SUPPLEMENTARY MATERIAL

To view all of the supplemental files associated with this article, visit www.biophysj.org.

We thank Peter Carlton, Emerick Gallego, Yuri Strukov, and Lifeng Xu for assistance with sample preparation.

This work was supported in part by the David and Lucile Packard Foundation, the Keck Laboratory for Advanced Microscopy, the Sandler Family Supporting Foundation, the National Institutes of Health (GM25101 to J.W.S., GM31627 to D.A.A.), the Burroughs Wellcome Fund's Interfaces in Science Program, the Wenner-Gren Foundation through a guest researcher fellowship to M.G.L.G., and by the National Science Foundation through the Center for Biophotonics, an NSF Science and Technology Center that is managed by the University of California, Davis, under Cooperative Agreement No. PHY 0120999.

REFERENCES

1. Hell, S., and E. H. K. Stelzer. 1992. Properties of a 4Pi confocal fluorescence microscope. *J. Opt. Soc. Am. A.* 9:2159–2166.
2. Schrader, M., and S. W. Hell. 1996. 4Pi-confocal images with axial superresolution. *J. Microsc.* 183:189–193.
3. Gustafsson, M. G. L., D. A. Agard, and J. W. Sedat. 1999. I^5M: 3D widefield light microscopy with better than 100 nm axial resolution. *J. Microsc.* 195:10–16.
4. Denk, W., J. H. Strickler, and W. W. Webb. 1990. 2-Photon laser scanning fluorescence microscopy. *Science.* 248:73–76.
5. Klar, T. A., S. Jakobs, M. Dyba, A. Egner, and S. W. Hell. 2000. Fluorescence microscopy with diffraction resolution barrier broken by stimulated emission. *Proc. Natl. Acad. Sci. USA.* 97:8206–8210.
6. Bailey, B., D. L. Farkas, D. L. Taylor, and F. Lanni. 1993. Enhancement of axial resolution in fluorescence microscopy by standing-wave excitation. *Nature.* 366:44–48.
7. Heintzmann, R., and C. Cremer. 1998. Laterally modulated excitation microscopy: improvement of resolution by using a diffraction grating. *Proc. SPIE.* 3568:185–195.
8. Gustafsson, M. G. L., D. A. Agard, and J. W. Sedat. 2000. Doubling the lateral resolution of wide-field fluorescence microscopy using structured illumination. *Proc. SPIE.* 3919:141–150.
9. Gustafsson, M. G. L. 2000. Surpassing the lateral resolution limit by a factor of two using structured illumination microscopy. *J. Microsc.* 198:82–87.
10. Frohn, J. T., H. F. Knapp, and A. Stemmer. 2000. True optical resolution beyond the Rayleigh limit achieved by standing wave illumination. *Proc. Natl. Acad. Sci. USA.* 97:7232–7236.
11. Frohn, J. T., H. F. Knapp, and A. Stemmer. 2001. Three-dimensional resolution enhancement in fluorescence microscopy by harmonic excitation. *Opt. Lett.* 26:828–830.
12. Gustafsson, M. G. L., L. Shao, P. M. Carlton, C. J. R. Wang, I. N. Golubovskaya, W. Z. Cande, D. A. Agard, and J. W. Sedat. 2008. Three-dimensional resolution doubling in wide-field fluorescence microscopy by structured illumination. *Biophys. J.* 94:4957–4970.
13. Graf, R., J. Rietdorf, and T. Zimmermann. 2005. Live cell spinning disk microscopy. *Adv. Biochem. Eng. Biotechnol.* 95:57–75.

14. Heintzmann, R., T. M. Jovin, and C. Cremer. 2002. Saturated patterned excitation microscopy—a concept for optical resolution improvement. *J. Opt. Soc. Am. A.* 19:1599–1609.

15. Gustafsson, M. G. L. 2005. Nonlinear structured-illumination microscopy: wide-field fluorescence imaging with theoretically unlimited resolution. *Proc. Natl. Acad. Sci. USA.* 102:13081–13086.

16. Schwentker, M. A., H. Bock, M. Hofmann, S. Jakobs, J. Bewersdorf, C. Eggeling, and S. W. Hell. 2007. Wide-field subdiffraction RESOLFT microscopy using fluorescent protein photoswitching. *Microsc. Res. Tech.* 70:269–280.

17. van Oijen, A. M., J. Köhler, J. Schmidt, M. Müller, and G. J. Brakenhoff. 1998. 3-Dimensional super-resolution by spectrally selective imaging. *Chem. Phys. Lett.* 292:183–187.

18. Betzig, E., G. H. Patterson, R. Sougrat, O. W. Lindwasser, S. Olenych, J. S. Bonifacino, M. W. Davidson, J. Lippincott-Schwartz, and H. F. Hess. 2006. Imaging intracellular fluorescent proteins at nanometer resolution. *Science.* 313:1642–1645.

19. Hess, S. T., T. P. Girirajan, and M. D. Mason. 2006. Ultra-high resolution imaging by fluorescence photoactivation localization microscopy. *Biophys. J.* 91:4258–4272.

20. Rust, J. M., M. Bates, and X. Zhuang. 2006. Sub-diffraction-limit imaging by stochastic optical reconstruction microscopy (STORM). *Nat. Methods.* 3:793–795.

21. Baldwin, J. E., and C. A. Haniff. 2002. The application of interferometry to optical astronomical imaging. *Philos. Trans. R. Soc. Lond. A.* 360:969–986.

22. Mitchison Laboratory protocols on fluorescence procedures for the actin and tubulin cytoskeleton in fixed cells. http://mitchison.med.harvard.edu/protocols/gen1.html.

23. Müller-Reichert, T., H. Hohenberg, E. T. O'Toole, and K. McDonald. 2003. Cryoimmobilization and three-dimensional visualization of *C. elegans* ultrastructure. *J. Microsc.* 212:71–80.

24. Staudt, T., M. C. Lang, R. Medda, J. Engelhardt, and S. W. Hell. 2007. 2,2′-thiodiethanol: a new water soluble mounting medium for high resolution optical microscopy. *Microsc. Res. Tech.* 70:1–9.

25. Hanser, B. M., M. G. L. Gustafsson, D. A. Agard, and J. W. Sedat. 2004. Phase-retrieved pupil functions in wide-field fluorescence microscopy. *J. Microsc.* 216:32–48.

26. Bewersdorf, J., R. Schmidt, and S. W. Hell. 2006. Comparison of I^5M and 4Pi-microscopy. *J. Microsc.* 222:105–117.

27. Lanni, F., D. L. Taylor, and A. S. Waggoner. Standing wave luminescence microscopy. US Patent 4,621,911. Filed 1985, issued 1986.

28. Gustafsson, M. G. L., D. A. Agard, and J. W. Sedat. Method and apparatus for three-dimensional microscopy with enhanced resolution. US Patent RE38,307E. Filed 1995, reissued 2003.

29. McNally, J. G., T. Karpova, J. Cooper, and J. A. Conchello. 1999. Three-dimensional imaging by deconvolution microscopy. *Methods.* 19:373–385.

30. Hell, S. W. 2007. Far-field optical nanoscopy. *Science.* 316:1153–1158.

31. Dyba, M., and S. W. Hell. 2002. Focal spots of size λ/23 open up far-field florescence microscopy at 33 nm axial resolution. *Phys. Rev. Lett.* 88:163901–163904.

32. Esa, A., P. Edelmann, G. Kreth, L. Trakhtenbrot, N. Amariglio, G. Rechavi, M. Hausmann, and C. Cremer. 2000. Three-dimensional spectral precision distance microscopy of chromatin nanostructures after triple-color DNA labeling: a study of the BCR region on chromosome 22 and the Philadelphia chromosome. *J. Microsc.* 199:96–105.

33. Gordon, M. P., T. Ha, and P. R. Selvin. 2004. Single-molecule high-resolution imaging with photobleaching. *Proc. Natl. Acad. Sci. USA.* 101:6462–6465.

34. Lidke, K. A., B. Rieger, T. M. Jovin, and R. Heintzmann. 2005. Superresolution by localization of quantum dots using blinking statistics. *Opt. Express.* 18:7052–7062.

35. Egner, A., S. Verrier, A. Goroshkov, H. Söling, and S. W. Hell. 2004. 4Pi-microscopy of the Golgi apparatus in live mammalian cells. *J. Struct. Biol.* 147:70–77.

36. Belmont, A. S., J. W. Sedat, and D. A. Agard. 1987. A three-dimensional approach to mitotic chromosome structure: evidence for a complex hierarchical organization. *J. Cell Biol.* 105:77–92.